

Electromagnetic Thermoforming to Manufacture Reflective Panels for Radio Telescopes and Downlinks

*Christian Davila-Peralta*¹
Justin Hyatt
Zack Hatfield
Alex St. Peter
Bailey S. Allen
Naomi Nguyen
Wyatt Ellis
Steward Observatory
Univ. of Arizona
Tucson, AZ 85721
¹cdavila@email.arizona.edu

*Dae Wook Kim*²
Joel Berkson
Emili Rodriguez
Wyant College of Optical
Sciences
Univ. of Arizona
Tucson, AZ 85721
²dkim@optics.arizona.edu

Abstract—Scientists of the Steward Observatory and Wyant College of Optical Sciences at the University of Arizona created a highly energy efficient adaptable method of forming precision freeform metal panels utilizing the combined effects of induction heating, electromagnetic force, an adjustable mold assembly, and infrared and visible metrology. This transformative component-level manufacturing technology has a broad application in industries requiring custom shaped high accuracy metal sheets (radio communication, automotive, aerospace, renewable energy, architecture).

fabricated using several reflective panels attached to a backing structure, forming parabolic shapes that are pointed to various points in the sky [1].

The main quality of a reflector antenna is described in terms of its aperture efficiency. The larger aperture efficiency, the smaller reflector diameter is required to achieve a given directive gain. This aperture efficiency can be factorized in several sub efficiencies that quantify different physical limitations [2].

One of the main contributors to gain loss in a telescope is the deviations from the ideal paraboloid shape. This is caused by several factors such as gravity load deformations, temperature gradients, and panels misalignments. Therefore, the reflective surface shape quality and stiffness is critical to antenna performance. Any deviation of the reflective surface shape from its ideal curvature introduces path length or phase errors in the receiver plane. The path length errors introduced are twice the effective surface errors. Path length errors in wavelength units represent phase errors. The wave front phase errors affect the radiation beam pattern in gain loss and increased sidelobe level [3].

For optimum and economic performance, the following four major contributors of the overall surface precision should roughly contribute equally. These contributions can be added in a root-sum-squared fashion, and each of them should not be larger than half the overall precision requirement [4]. These factors are as listed:

- (1) The fabrication precision of each individual panel composing the reflector surface.
- (2) The alignment of the panels to the desired reflector profile.
- (3) Gravitational deformation of the reflector's backup structure with elevation angle.
- (4) The influence of temperature variations and wind forces.,

TABLE OF CONTENTS

1. INTRODUCTION.....	1
2. REFLECTING PANELS MANUFACTURING.....	2
3. ELECTROMAGNETIC THERMOFORMING	3
4. EXPERIMENTAL SETUP	6
5. ADJUSTABLE MOLD	10
6. SURFACE METROLOGY	12
SUMMARY	13
ACKNOWLEDGEMENTS	13
REFERENCES.....	13
BIOGRAPHY	14

1. INTRODUCTION

A radio telescope is a device used to collect radio waves from astronomical radio sources in the sky. This is the main observing instrument used in radio astronomy, which studies the radio frequency portion (from 20 KHz to 300 GHz) of the electromagnetic spectrum emitted by astronomical objects. This is comparable to the use of optical telescopes in optical astronomy. Radio telescopes are typically large parabolic antennas, like the ones used in communications with satellites and space probes, that are used independently or linked together electronically in an array, with the advantage of performing observations during the day unlike optical telescopes. Since the wavelengths used are longer, radio telescopes require large antennas (10 m to 300 m in diameter) to collect enough radio energy to study them. For this reason, a radio antenna's main (primary) reflectors are typically

978-1-7281-7436-5/21/\$31.00 ©2021 IEEE

The reflector panel design plays a very important role in the telescope construction and operation. In order to achieve higher frequencies, new cost-effective manufacturing methods have to be developed.

2. REFLECTING PANELS MANUFACTURING

In large telescopes, the main reflector is made of curved segments called panels, which placed together form the parent shape (commonly a paraboloid) of the primary reflector. Different methods have been used to manufacture high precision (<.5 mm Root Mean Square or RMS) panels with compound curvatures. Techniques like machining, stretching (aluminum cassette) and electroforming are among the most popular and have been used since the 1950's for different designs [4], with different precision specifications depending on the frequency range that the telescope is designed for as shown in Table 1.

Table 1. Panel manufacturing technologies [4].

Type	Example	Precision ($\mu\text{m rms}$)	Max. size (m)
Aluminum cassette	Effelsberg	>80	2.5
CFRP sandwich	MRT HHT	25	1.2
Machined aluminum	ALMA US	<10	0.8
Electroformed nickel	ALMA EU	<10	1.2

Machining

Regarding the machining method, a thick slab of material (typically aluminum) is machined in several steps, involving the removal of material to form a backing structure with a coarse milling tool, and the formation of a compound curve in the opposite face using a rough milling process. The backing structure provides the stiffness and stability required. The next step is measuring the panel then fine machining the reflective surface using grinding techniques. Very high precision can be obtained with this method (<5 $\mu\text{m RMS}$), and further treatment can be applied to the reflective surface (i.e. acid etching) to reduce its reflectivity of undesired wavelengths (i.e. visible or infrared sunlight). Mitsubishi used this method to manufacture the Japanese ALMA telescope panels, and the German company Zrinski made the North American ALMA panels [4, Baars]. Although this method is known for its precision, its cost and time consumption are prohibitive for the majority of radio telescope primary reflectors and is reserved only for the high frequency ones (<100 GHz) or for the secondary reflector in some other cases [5].

Electroforming

The radio reflective panels developed by the Italian company Media Lario applies the so-called electroforming technology to produce high accuracy and satisfactory radio frequency performance. The process starts with the production of a negative mold where the reflective skin of the panel will be deposited. This mold can be machined out of a conductive blank, or glass can be polished to achieve higher accuracy (with the following addition of a conductive layer). The mold is then inserted into a proprietary electrolytic bath while a charge is induced in the mold, serving as the anode of an electrolysis process. The cathode is a nickel blanket that is deposited onto the anode forming a skin that can grow up to 0.6 mm, replicating the external shape of the mold with micrometer accuracy. This nickel paneling has achieved surface accuracy down to 10 $\mu\text{m RMS}$, with a peak to valley of 49.6 μm and surface roughness of 0.16 μm . [6, Valsecchi] Electroforming radio telescope panels is an elegant solution, but is expensive and time consuming. The series production is possible using a single mold, but having different shapes requires the machining of different molds and the use of dangerous chemicals requiring special methods for disposal. The dimension of the manufacture's production facilities limits the panel size to 1.2 m per side [4].

Aluminum cassette

Another method available is stretching (aluminum cassettes), which is produced by several fabricators in sizes up to 2.5 m, and precision upwards of 80 $\mu\text{m RMS}$. According to Baars [4], the size limit is driven by shipping and handling parameters, not by limitations in the manufacturing method. These panels are produced in an economic way on universal jigs, adaptable to the required shapes. Companies that commercialize these panels use a mold with holes connected to vacuum lines, that will later hold in position a thin aluminum sheet. This sheet will have been treated to increase the anchor profile with an anodizing method to ensure the glue bonds to the ribs. These ribs are formed with aluminum Z profiles, having vertical cuts to increase its flexibility. Once the aluminum sheet is held against the mold by vacuum, operators place glue on to it to attach ribs manually before weight is added to the ribs to help hold them in place. Several hours later, when the glue has cured, the vacuum is released and the panel is now held in position by the glued ribs, although some spring back will be present. The panel is then placed in a photogrammetry assembly to check for shape deviations.

Carbon Fiber Reinforce Plastic

Panels have also been made by laying carbon fiber reinforced plastic (CFRP) on a cast iron or glass mold. Thin CFRP sheets are bonded to the top and bottom of an aluminum honeycomb core to form a rigid panel. The top sheet of each panel includes a metallic layer to provide reflectivity. These methods were developed in the construction phase of Effelsberg, MRT and IRAM telescopes. The molds are expensive and economically competitive only in mass

production of panels of the same shape. The achieved panel shape error is about twice that of the mold [4].

3. ELECTROMAGNETIC THERMOFORMING

A new process to produce compound curve metal panels is being developed at the University of Arizona [6], with applications in several industries (Table 2), including sub millimeter radio telescope reflectors and downlinks. The so-called induction thermoforming utilizes a hybrid effect of localized induction heating (Joule effect) and electromagnetic (EM) force (Lorentz effect) to heat and press the panel at the same time along the non-contact “tool” path controlled by a Computer Numerical Control (CNC) machine as depicted in Figure 1.

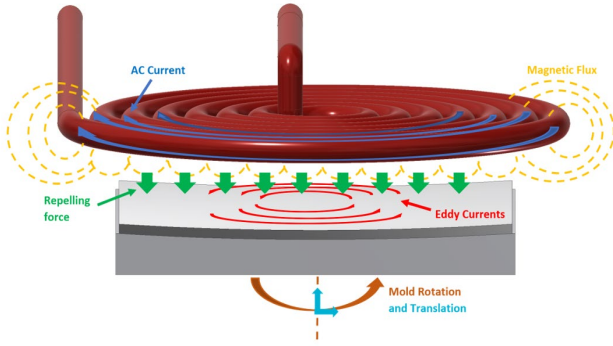


Figure 1. Induction thermoforming diagram: a pancake induction coil induces a current in the work piece, heating it and pressing it towards the mold, which is rotating to ensure an even distribution of the heat.

A simple way to describe the induction-based thermoforming process is in terms of energy transformation. Electric power from the utility is converted using an induction power supply whose output has an RLC (Resistor: R, Inductor: L, and Capacitor: C) circuit to provide power to the induction coil. To prevent impedance losses in the circuit, the frequency induced in the coil must be the same as the resonant frequency of the RLC circuit. The resonance of a circuit occurs when the inductive and capacitive reactance are equal in magnitude but cancel each other because they are 180 degrees apart in phase.

$$\omega_0 = \frac{1}{\sqrt{LC}} \quad (1)$$

Where ω_0 is the resonant angular frequency, L is the coil inductance and C and the capacitance. The alternating current in the pancake induction coil (used by the thermoforming process) will produce a strong magnetic field around its turns, by means of the Biot-Savart law.

$$B = \frac{\mu_0 I}{4\pi} \oint \frac{ds \times (P - s)}{|P - s|^3} \quad (2)$$

Where \mathbf{B} is the magnetic field, μ_0 vacuum permeability, \mathbf{I} is the current through the coil, \mathbf{P} is the vector normal to the plane of the coil, \mathbf{s} is a vector pointing to the centerline element of the coil conductor ds . Conversely, a time-varying external magnetic flux induces currents in a conductor such as the WP placed near the coil, due to Faraday's law of induction:

$$\oint_C \mathbf{B} \cdot d\mathbf{l} = \mu_0 \iint_S \mathbf{J} \cdot d\mathbf{S} = \mu_0 I_{enc} \quad (3)$$

Where \mathbf{J} is the total current density (in amperes per square meter), $d\mathbf{l}$ is the infinitesimal element of curve C , $d\mathbf{S}$ is the vector area of an infinitesimal element of surface S , I_{enc} is the total current passing through a surface S enclosed by C , μ_0 is the vacuum permeability, and \mathbf{B} is the magnetic field. The currents created in the WP are called eddy currents. Due to Ampere's law, the circular eddy currents create a counter magnetic field, causing a repulsive force between the WP and the induction coil. This force has been modeled in terms of two concentric spiral currents separated a distance \mathbf{z} from each other. The force experienced between the coil and the WP is:

$$F = I_{WP} \oint_C d\mathbf{l}_{wp} \times B \quad (4)$$

Where $d\mathbf{l}$ is longitudinal differential component in the coil spiral, \mathbf{F} the force experienced between the coil and the WP, and \mathbf{I}_{wp} the eddy current in the WP. One of the novelties of the proposed induction thermoforming is that the repulsive force will press and shape of the WP.

At the same time, the eddy currents in the WP heat it up due the Joule effect,

$$P = \frac{\pi^2 B_p^2 d^2 f^2}{6\rho D} \quad (5)$$

where \mathbf{P} is thermal power per unit mass, \mathbf{B}_p is the peak magnetic field, \mathbf{d} is the thickness of the WP, \mathbf{f} is the frequency, ρ is the resistivity of the WP material, and \mathbf{D} is the density of the material. By this mechanism, the WP is substantially heated, hence reducing its yield strength. This makes it possible for it to be plastically deformed using a smaller force (i.e., the repulsive force created by opposite currents in the induction coil and WP).

In order to fully understand the operation mechanism of this multiphysics phenomena, it was split into different processes for which several analytical and empirical equations have been developed. These different processes were then coupled in a simulation environment using computational tools.

Metal high temperature softening

The electromagnetic thermoforming process uses the high temperature softening phenomena of metals (e.g. aluminum) as a first step, where a yield strength reduction is observed as function of temperature, to perform plastic deformation with reduced force and spring back, similar to a hot stamping processes [7].

Several approximations have been proposed to characterize the relationship between strain rate, stress and temperature, such as the modified Arrhenius constitutive equation one that directly relates the three of them. The Zener-Hollomon equation parameter Z describes the effects of the strain rate and temperature on the thermal deformation behavior. The hyperbolic sine Arrhenius-type equation provides a better approximation between the Z parameter and the stress, and is described as follows:

$$\begin{aligned} Z &= \dot{\epsilon} e^{\left(\frac{Q}{RT}\right)} & (6) \\ Z &= A_1 \sigma^{n_1} & (7) \\ Z &= A_2 e^{(\beta\sigma)} & (8) \\ Z &= A(\sinh(\alpha\sigma)^n) & (9) \\ \alpha &= \frac{\beta}{n_1} & (10) \end{aligned}$$

Where $\dot{\epsilon}$ is the strain rate, R the universal gas constant, T the absolute temperature, Q the activation energy, σ flow stress and A_1 , A_2 , A , α , β , n_1 , n are material constants. Equations (7) and (8) describe the lower and higher flow stress conditions, and they are unified in equation (9), although it lacks any physical meaning. Combining equations (6) and (9), the Arrhenius constitutive equation can be expressed:

$$\dot{\epsilon} = A(\sinh(\alpha\sigma)^n) e^{\left(\frac{Q}{RT}\right)} \quad (11)$$

As shown by Liu [7], taking the logarithm on both sides of simultaneous equations (6) and (7), equations (6) and (8), respectively, the following equations can be attained:

$$\ln(\sigma) = \frac{\ln(\dot{\epsilon})}{n_1} - \frac{\ln(A_1)}{n_2} + \frac{Q}{n_1 RT} \quad (12)$$

$$\sigma = \frac{\ln(\dot{\epsilon})}{\beta} - \frac{\ln(A_2)}{\beta} + \frac{Q}{\beta RT} \quad (13)$$

$$\ln(\sinh(\alpha\sigma)) = \frac{\ln(\dot{\epsilon})}{n} - \frac{\ln(A)}{n} + \frac{Q}{nRT} \quad (14)$$

The material coefficients n_1 , β , n , Q , and A are to be obtained by linear fittings of equations (12) to (14), and α could be obtained through equation (10) and use them as a function of the strain ϵ , using the experimental data as Liu [7]. Finally, the constitutive relationship is expressed as:

$$\sigma = \frac{1}{\alpha} \operatorname{arcsinh} \left(e^{\left(\frac{\ln(\dot{\epsilon}) - \ln(A) + \frac{Q}{RT}}{n} \right)} \right) \quad (15)$$

Induction heating

The mathematical model developed for induction heating normally involves three main physical phenomena related to electromagnetism, heat transfer, and solid mechanics [8]. The global system of equations for modeling electromagnetic wave propagation is based on the four Maxwell equations:

$$\vec{\nabla} \cdot \vec{B} = 0 \quad (16)$$

$$\vec{\nabla} \cdot \epsilon \vec{E} = 0 \quad (17)$$

$$\vec{\nabla} \times \vec{E} = -\frac{\partial \vec{B}}{\partial t} \quad (18)$$

$$\vec{\nabla} \times \vec{H} = \vec{j} + \frac{\partial \epsilon \vec{E}}{\partial t} \quad (19)$$

Where \mathbf{B} is the magnetic flux density, \mathbf{H} the magnetic field strength, ϵ is the dielectric constant, \mathbf{E} the electric field, and \mathbf{j} the electric current density. The system of equations can be coupled with relations associated to material properties:

$$\mu(T, |\vec{H}|) = \frac{\partial \vec{B}}{\partial \vec{H}} \quad (20)$$

$$\vec{j} = \sigma(T) \vec{E} \quad (21)$$

Where μ is the differential magnetic permeability, σ is the electrical conductivity and T the temperature. The electromagnetic resolution consists of calculating fields, $\mathbf{E}(\mathbf{r}, \mathbf{t})$, $\mathbf{B}(\mathbf{r}, \mathbf{t})$, $\mathbf{H}(\mathbf{r}, \mathbf{t})$ and $\mathbf{j}(\mathbf{r}, \mathbf{t})$ at any location \mathbf{r} and time \mathbf{t} that satisfy all equations (19) to (21). Favenecc [8] proposed to write a single second-order wave propagation-like equation. When solving the electromagnetic problem using the electrical field for instance, the procedure is the following. By dividing (18) by the differential magnetic permeability (20) and taking its rotational on both sides, one gets:

$$\begin{aligned}\vec{\nabla} \times \left(\frac{1}{\mu} \vec{\nabla} \times \vec{E} \right) &= -\vec{\nabla} \times \frac{\partial \vec{H}}{\partial t} \\ &= -\frac{\partial}{\partial x} (\vec{\nabla} \times \vec{H})\end{aligned}\quad (22)$$

Substituting (19) into (7) gives:

$$\frac{\partial}{\partial t} \left(\vec{j} + \frac{\partial \varepsilon \vec{E}}{\partial t} \right) + \vec{\nabla} \times \left(\frac{1}{\mu} \vec{\nabla} \times \vec{E} \right) = 0 \quad (23)$$

The total current density \mathbf{j} is the sum of the induced currents $\sigma \mathbf{E}$ and the imposed one \mathbf{J}_s , (23) becomes into (24) when introducing the Ohm law (21):

$$\varepsilon \frac{\partial^2 \vec{E}}{\partial t^2} + \sigma \frac{\partial \vec{E}}{\partial t} + \vec{\nabla} \times \left(\frac{1}{\mu} \vec{\nabla} \times \vec{E} \right) = -\frac{\partial \vec{J}_s}{\partial t} \quad (24)$$

With the electrical field as the unknown, the electromagnetic problem consists of calculating $\mathbf{E}(\mathbf{r}, \mathbf{t})$, and satisfying (24) along with the null divergence condition (17). In the same manner, the electromagnetic problem results in, when using the magnetic field $\mathbf{H}(\mathbf{r}, \mathbf{t})$ as the unknown, calculating $\mathbf{H}(\mathbf{r}, \mathbf{t})$ while satisfying (25) and its null divergence condition (16):

$$\varepsilon \frac{\partial^2 \vec{H}}{\partial t^2} + \sigma \frac{\partial \vec{H}}{\partial t} + \vec{\nabla} \times \left(\frac{1}{\mu} \vec{\nabla} \times \vec{H} \right) = -\frac{\partial \vec{J}_s}{\partial t} \quad (25)$$

Previous work has been done to simplify this equation using axis-symmetrical configurations, changing the coordinate system to cylindrical coordinates, and neglecting terms that will change the wave propagation into a diffusion like equation, that is easy to handle. This simplification works for solenoid type coils, where the working piece is inside the solenoid. Additional work will be required to solve the equation, taking into consideration the use of a pancake coil.

Heat transfer in the work piece

The heat transfer equation can be used to describe the heat transfer model. The eddy currents generated in the work sheet, and derived in the electromagnetic model, will induce the heat dissipation within the work piece [9].

$$\rho C \frac{\partial T}{\partial t} - \text{div}(k \vec{\nabla} T) = \sigma E^2 \quad (26)$$

Where ρ is the material density, C the specific heat, k the thermal conductivity, and σE^2 is the Heat source term due to eddy currents. The specific heat and thermal conductivities are temperature dependent. As for the boundary conditions, different kinds for temperature, or its normal derivative can

be prescribed at the interfaces, like convection and radiation between the workpiece and its surroundings:

$$-k \vec{\nabla} T \cdot \vec{n} = h(T - T_{ext}) + \varepsilon_{emi} \sigma_{ste} (T^4 - T_{ext}^4) \quad (27)$$

$$-k \vec{\nabla} T \cdot \vec{n} = \phi_{pres} \quad (28)$$

$$T = T_{pres} \quad (29)$$

Where n is the outward unit normal vector, h is the convective heat transfer coefficient, ε_{emi} the workpiece emissivity, σ_{ste} the Stephan-Boltzmann constant, and T_{ext} the room temperature.

Electromagnetic forming

A further step in the induction thermoforming process is similar to the process known as electromagnetic forming, where a pulsed magnetic field is used to apply Lorentz forces to workpieces made of highly conductive material without mechanical contact [10]. This process is a high-speed forming (impulse), based on the physical effects described by Maxell in 1873, which explained that a temporarily varying magnetic field induces electrical currents in nearby conductors and additionally exerts forces to these conductors. For its mathematical description of the phenomena, one can start with the Lorentz formula:

$$\vec{F} = \vec{j} \times \vec{B} \quad (30)$$

Where \mathbf{F} is the volume forces acting in the workpiece, \mathbf{J} is the current density, and \mathbf{B} the magnetic flux density. The current density equals the negative derivative of the magnetic field strength \mathbf{H} with respect to the z coordinate (parallel to the workpiece thickness):

$$\vec{j} = -\frac{\partial \mathbf{H}}{\partial z} \quad (31)$$

The magnetic flux density is the result of the product of the permeability μ and the magnetic field strength \mathbf{H} . Hence, the forces acting on a sheet metal workpiece can be calculated:

$$F_z = -\mu H \frac{\partial H}{\partial z} = -\frac{1}{2} \mu \frac{\partial (H^2)}{\partial z} \quad (32)$$

This volume forces acting on the workpiece can be transformed into a virtual surface force, called magnetic pressure. According to Bhuler [11] the pressure difference between two points in the wall of the workpiece can be determined by integrating the acting forces over the distance. Using the lower and upper surface of the workpiece as integration limits. The magnetic pressure depends only on the magnetic field strength in the gap between the tool coil and workpiece \mathbf{H}_{gap} and on the penetrated magnetic field \mathbf{H}_{pen} .

$$p(t) = \frac{1}{2} \mu H_{gap}^2(t) \quad (33)$$

Where $\mathbf{p}(\mathbf{z},t)$ is the magnetic pressure, \mathbf{H}_{gap} is the magnetic field strength in the gap, and \mathbf{H}_{pen} the magnetic field strength that penetrates.

If the skin depth is small in comparison to the thickness of the workpiece, as is common in high frequency applications that the penetrated magnetic field can be neglected, and the magnetic pressure can be calculated by using the simplified version:

$$p(z, t) = \int_{z_0}^{z_i} F(z, t) dz \quad (34)$$

$$= \frac{1}{2} \mu (H_{gap}^2(t) - H_{pen}^2(t))$$

This simplification is valid only if the wall thickness equals at least 1.5 times the skin depth. The skin depth is a function of the frequency and the resistivity of the workpiece material and can be calculated as follows [12]:

$$\delta = \sqrt{\frac{\rho}{\pi f \mu}} \quad (35)$$

Where, δ is the skin depth, ρ is the workpiece resistivity, f is the current density and μ the vacuum permeability.

Although the induction thermoforming process can use the same equations to describe the forces acting in the workpiece






during the electromagnetic formation, there are key differences that make induction thermoforming different. In induction thermoforming, the workpiece is heated first to lower the yield strength. As opposed to the electromagnetic formation where a very high energy pulse is induced in the workpiece to quickly deform it, the induction process slowly deforms the piece, applying lower forces in a two-step process that can be repeated several times. During induction thermoforming, the coil scans the workpieces to evenly distribute the temperature along it. This capability allows for work to be carried out with bigger workpieces using a small tooling coil. The deformation in the thermoforming technology is analog to the incremental forming, as the deformation in the electromagnetic forming is made in quick fashion, analog to stamping. Induction thermoforming can control the cooling of the workpiece by slowly and selectively applying power to some sections of it. This is useful for thermal treatment of the workpiece.

4. EXPERIMENTAL SETUP

The first experiments were performed using a 15 kW (Figure 3) induction power supply originally designed to operate with a small solenoid coil, used in ironwork and melting operations. The operation characteristics of the power supply are described in table 4. The water-cooled power supply requires a water inlet to cool the electronics and induction coil, and a heat dumping mechanism, which was made with a car radiator and a water pump. The required heat dump capacity required is <15 kW, which was easily obtained with the car radiator (TYC 2298, Chrysler PT Cruiser 2009) that is designed to operate at much elevated rates (~150 Hp).

The size of the inductor coil is limited by the frequency range of the power supply. The inductance on the pancake coil can be calculated with the following empirical equations [13]:

Table 2. Electromagnetic Thermoforming application analysis in different industries [4].

Industry	Piece type	Advantages of Induction Thermoforming	Picture
Radio communication	Antenna panels	High frequency, prototypes, off-axis capability, low energy footprint.	
Concentrated solar power	Reflective panels	High strength panels, high accuracy dish shapes, off axis capability, high and low sags, low energy footprint.	
Aerospace	Wings panels, Fuselage shell panels	Short runs capability, controlled strength, different shapes, low NRE cost, reduced energy footprint.	
Automotive	Hood, ceiling, trunk lid, etc.	Prototype capability, energy efficient.	
Architecture	Exterior and interior façade walls	Artistic forms capability, different shapes capability, short runs	

$$L = \frac{N^2 A^2}{30A - 11D_i} \quad (36)$$

$$A = \frac{D_i + N(W + S)}{2} \quad (37)$$

Where, **L** is the coil inductance (μH), **D_i** is the inner diameter (in), **N** is the number of turns, **W** is the conductor diameter (in), and **S** is the turn spacing (in). Hence, for a fixed cross-sectional area, the number of turns increases the inductance to the square in the flat spiral coil, reducing the resonant frequency as shown in equation (1). After experimenting with different coil sizes, the configuration in figure 2 below resonated at a frequency of 35 kHz.



Figure 2. CAD drawing representing the coil used in the initial experiments with 7 turns made from a flexible cooper tube which cross section has 8 mm external diameter and 1 mm thickness, a 1 mm thick fiberglass jacket was used as electrical insulation.

A glass mica ceramic mold was machined with one face having a convex spherical surface with radius of 1410 mm, and dimension of 125 x 125 x 12 mm. After machining, the mold was scanned using a Coordinate Measurement Machine (CMM) to check the RMS error to the prescribed parabola. The cloud point was made from 25 points across the spherical surface, fitted into plane with the following equation:

$$z(x, y) = a(x^2 + y^2) + bx + cy + d \quad (38)$$

$$a = \frac{1}{4f} \quad (39)$$

Where **f** is the focal length of the parabola, equivalent to half of the radius of a sphere. In order to test the measurement precision and method, five independent measurements were taken of the mold, making a cloud of 25 points (Figure 4). This cloud point where analyzed and fitted into equation (38), with the term $a = 3.5461 \times 10^{-04}$, having a 65 μm RMS error.

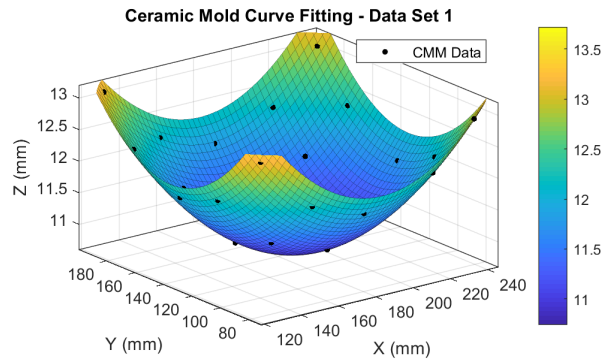


Figure 4. Curve fitting of the first data set, having a 0.0065 mm RMS error



Figure 3. HT-15KW induction power supply with a small solenoid used in home ironwork process (left), pancake induction coil placed in the same power supply on top of the workpiece and ceramic mold (right).

To account for the heating power, a control mass analysis was developed to account for heat losses. Considering the aluminum plate (125x125x3 mm, 1100 allow) as isothermally heated, and ignoring thermal losses in the vertical edges, the following closed system model was used.

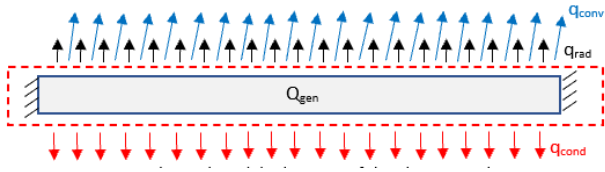


Figure 5. Lumped capacitance transient thermal model schematic of the aluminum plate, accounting for radiative and convective losses on top face, and conduction losses on the bottom face. Loses on the vertical faces are ignored and a even distributed heat source is supposed in the plate body.

$$-mC \frac{dT}{dt} = \dot{Q}_{gen} - \dot{q}_{rad} - \dot{q}_{conv} - \dot{q}_{cond} \quad (40)$$

$$\dot{q}_{rad} = \varepsilon\sigma A(T^4 - T_{air}^4) \quad (41)$$

$$\dot{q}_{conv} = hA(T - T_{air}) \quad (42)$$

$$\dot{q}_{cond} = \frac{1}{R_{th}}(T - T_{air}) \quad (43)$$

Where m , is the mass of the workpiece, C is the specific heat, T workpiece temperature, T_{∞} is room temperature, Q_{gen} generated heat, A is the area of the upper or bottom faces, ε is the emissivity coefficient of the plate, σ Stephan-Boltzmann constant, h the average convective heat transfer coefficient, k the ceramic mold thermal conductivity coefficient, and z the mold thickness.

In equations (40-43) the emissivity, convection and conductivity coefficients are temperature dependent terms, and their dependence must be calculated. The conduction heat loss also depends on the contact resistance, which had to be considered in the loses estimation as well as the mold heat resistance, and down facing convection resistance. Accounting for radiation heat loss, previous studies report oxidized aluminum total emissivity measurements slightly increase with temperature from 0.113 at 473 K to 0.192 at 873 K for an initially polished aluminum sample. In the other hand, natural convection (slow rotation of the workpiece) or forced convection (at higher rotation speeds) can add an important loss that requires further study.

A first an experiment to estimate the heating power of the induction setup was designed to measure the temperature of the plate rotating underneath the induction coil, placed at 3 mm above the induction coil. The data obtained is depicted in Figure 6.

To estimate the power, the dT/dt term was obtained from the linear portion of the temperature rising curve and multiplied by the mass and heat capacity of aluminum, obtaining an estimated of 230 watts. The current and voltage in the coil was also measured at the time of the experiment, having a current of 300 A and a voltage 4.41 V. The heating efficiency in this configuration was 17%.

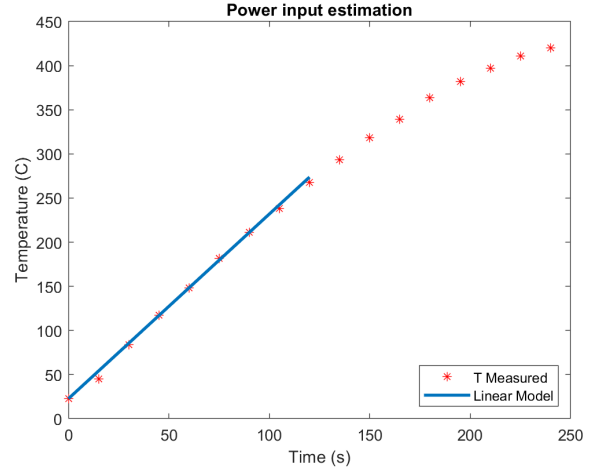


Figure 6. Plate measured temperature and heat generation estimation in the linear portion of the transient curve, showing a heat generation of 230 W.

In a different experiment, the repelling force was also measured for different currents and different distances, using a flat plate of aluminum (125 x 125 x 3 mm, Al 1100). The resulting maximum measured at 4.47 N, when the work plate was placed in 1 mm from the induction coil with a current of 353 A. Force was proportional to the current and to the distance between the coil and the workplate as shown in Figure 7.

The next part of the experiment was to perform a slumping process in this shape. A two-step routine was performed in the slumping process, using 99 seconds of moderate power to heat up the plate and 12 seconds at full power to press it into the mold as depicted in Figure 8. The process was repeated 12 cycles to obtain a slumped piece.

After the thermoforming process, the slumped panel was measured in a CMM to determine the shape quality. In a first analysis, the panel shape was compared to the one of the mold (Figure 9). The results showed a 94 um RMS difference between the shape of the ceramic mold and the shape of the panel (Table 3). Analyzing the shape of the residual plot (Figure 10), it is clear that a spring back effect is altering the shape accuracy.

In a second analysis, a best fit curve was performed to estimate a change in the radius of curvature caused by a spring back effect, which resulted in a 45 um RMS error with a radius of curvature of 1621.8 mm compared with the 1410 mm prescribed radius of the mold. The results are shown in Figure 11, 12 and table 4.

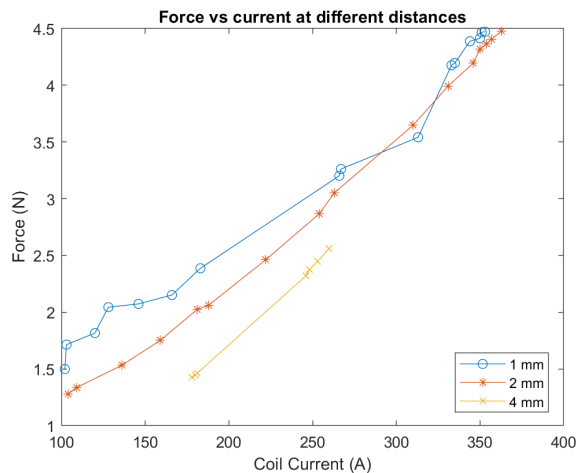


Figure 7. Force data obtained at different coil currents and distances between the coil and the work plate, after 4 mm the resonant frequency drop under the machine limits (> 30 kHz).

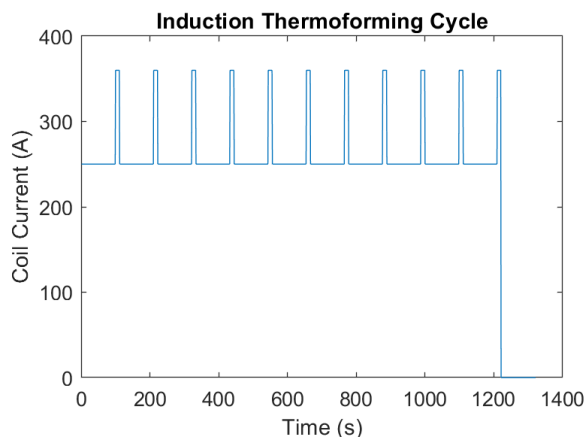


Figure 8. Thermoforming cycle repeated 11 times, using both, the heating effect during the low power part of the cycle and the electromagnetic pressure in the high part of the cycle. The time cycle was determined experimentally and limited with the induction power supply capabilities.

Different polynomials were also analyzed to determine the source of error, table 9 shows the result of the fitting with a second order polynomial. The slight difference between the a and b terms shows a slight change in the focal length of the parabola against the x and y axis, probably caused by an anisotropic behavior of the aluminum plate, but the results are yet to be confirmed. A ray trace analysis may be performed in the future to determine the impact of the a, b, and c terms in the quality of the reflected image. Using this polynomial, the RMSE drops to 31 μm .

Table 3. Curve fit output of the slumped panel compared to a similar curve than the mold, dimensions in millimeters.

General model:	$f(x,y) = a*(x^2+y^2)+b*x+c*y+d$
Coefficients (with 95% confidence bounds):	
a	3.5461e-04
b	-0.08314 (-0.0833, -0.08297)
c	-0.08037 (-0.08055, -0.0802)
d	-453.5 (-453.6, -453.5)
Goodness of fit:	
SSE:	6.079
R-square:	0.9716
Adjusted R-square:	0.9715
RMSE:	0.0942

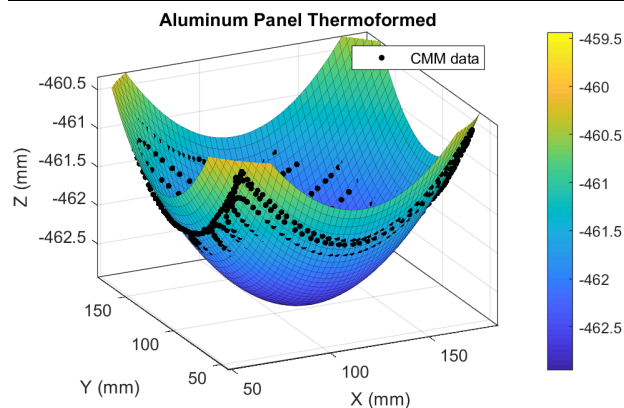


Figure 9. Curve fitting of the slumped panel to a similar curve than the mold.

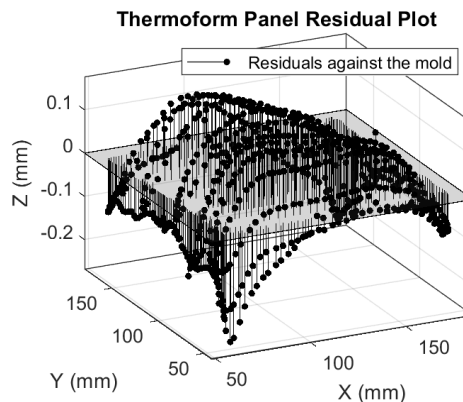


Figure 10. Residual plot of the slumped panel to a similar curve than the mold.

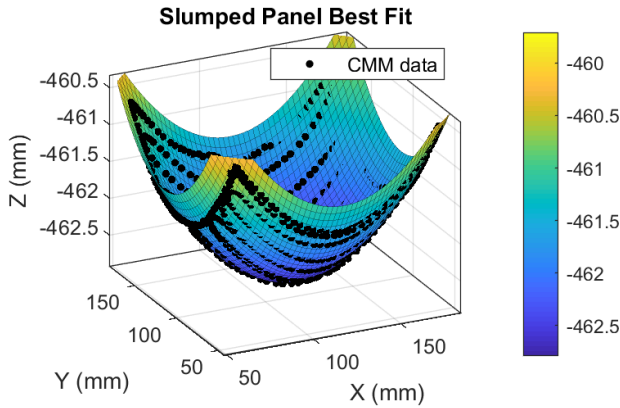


Figure 11. Curve fitting plot of the slumped panel to a best fit curve.

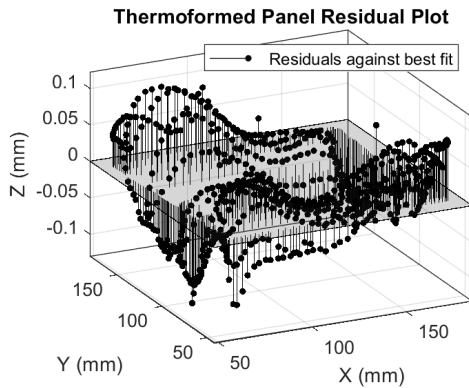


Figure 12. Residual plot of the slumped panel to a best fit curve.

Table 4. Curve fit output of the slumped panel compared to a similar curve than the mold, dimensions in millimeters.

General model:	$f(x,y) = a*(x^2+y^2)+b*x+c*y+d$
Coefficients (with 95% confidence bounds):	
a	0.0003083 (0.0003063, 0.0003102)
b	-0.07237 (-0.07282, -0.07192)
c	-0.07015 (-0.07058, -0.06972)
d	-454.6 (-454.6, -454.5)
Goodness of fit:	
SSE:	1.413
R-square:	0.9934
Adjusted R-square:	0.9934
RMSE:	0.04545

5. ADJUSTABLE MOLD

A significant non-recurring cost (NRC) of producing goods with methods like stamping, hot stamping and electroforming is the mold manufacturing. In cold forming operations of high strength metal sheets, severe tool damage and large spring backs are problematic [14]. The die must be designed to compensate this spring back and its often machined in an expensive and time-consuming process that limits their use industrial series production.

A solution to the for mentioned problems was developed and described in a patent by Dr. Roger Angel [15], where a plurality of tiles are precisely manipulated by 3 micrometer actuators forming an arbitrary shape (i.e. a parabola used to produce concentrating mirrors). A new technology that evolved from that idea was developed and proposed to be used with the induction thermoforming technology [16].



Figure 13. Adjustable mold: 50 x 50 cm prototype with bolts used as actuators adjusted from the back.

The ‘adjustable mold’ is comprised of a flexure, a metallic sheet cut in a way that dramatically increases its flexibility. This flexure may be described as a plurality of hexagonal tiles, joined with springs, forming a honeycomb pattern that can be conformed to a discrete version of an arbitrary surface inside the elastic region of deformation. Several of these tiles have an actuator that sets the z position of the central part of such tile. This actuator is joined to the tile with a swivel like mechanism that allows free tilting of the hexagons. A rigid frame of the system engages a plurality of actuators in a way that allows the actuators to move in axial direction. The shape of this adjustable mold is obtained setting the correct Z position of each tile, which is influenced by the position of their neighbor tiles, and tilting it directionally to be able to form a smooth surface.

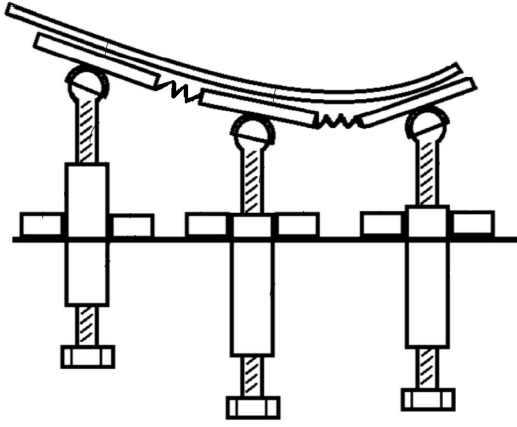


Figure 14. Adjustable mold showing the tiles joined with springs forming a segmented version of the desired shape, and the workpiece being formed on top of it

The process to adjust the mold uses the help of a coordinate measuring machine (CMM), who's output is a 3D cloud point of the position of the center of each tile. This cloud point is processed by an algorithm created in Matlab where a custom equation (i.e. the parabolic equation of the desired shape) is compared with the point cloud (Figure 15a). The algorithm then converts the residuals plot (Figure 15b) into degrees, and turns directions of each actuator, to print in a position matrix. This matrix is then used by the operator to perform a new iteration to adjust the mold by individually adjusting (rotating) each actuator by a close approximation to the prescribed amount. The tool used for adjustment was a simple Alan-key and protractor combination, where the angular adjustment resolution per actuator was limited by the resolution of the protractor and fidelity of the Alan-key (estimated at about 5 degrees or 18 microns of z-travel). A more sophisticated adjustment tool technology is currently under development however, the results below reflect what was accomplished with the tool described. Figure 15 (c)

shows a chart comparing the RMS obtained versus the iteration, showing that a 56 μm RMS could be obtained in around 7 iterations, while an exponential fitting shows the trend.

The minimum RMS achievable is a function of the size of the adjustable mold, the surface characteristics and the size of each tile that conform the flexure. If, for example, the desired shape is a parabola with vertex in the center of the mold, a simple comparison between the parabola segment covered by the hexagonal tile in the center can give a closed approximation. The RMS error formula described below, where Z_{mi} is the i^{th} measured sample, and Z_{pi} is the expected value of the i^{th} position (i.e. specific x and y position), and n the number of samples:

$$RMSe = \sqrt{\frac{\sum_{i=1}^n (z_{mi} - z_{pi})^2}{n}} \quad (44)$$

A Matlab code was developed to account for the difference RMS error, considering the differences from an asymmetric parabola surface with focal length f , with equation:

$$z(x, y) = \frac{1}{4f} (x^2 + y^2) \quad (45)$$

And a square tile (for simplifying purposes) placed in the $z=0$ plane, with an arbitrary size. The results are shown in figure 16 where the minimum RMS error exponentially decreases with the focal length of the parabola. For a fixed focal length, the RMS error is minimized when reducing the tile size as expected. This approach is conservative as the tiles are considered a square, where the real ones used are hexagonal. On the other hand, the plane analyzed could be $z(x, y) \neq 0$, a plane called the least square plane that minimizes the RMSE.

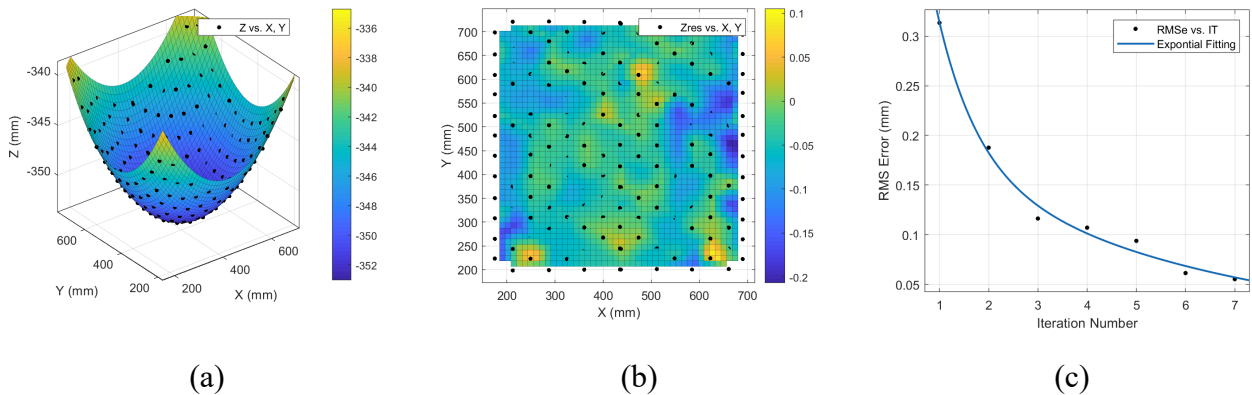


Figure 15. Adjustable mold fine tuning: a) point cloud for the final iteration, with the second order polynomial curve fitting; b) residual plot for the required curve and c) iteration vs RMS error for a desired curve, obtaining 56 μm RMS in 7 iterations.

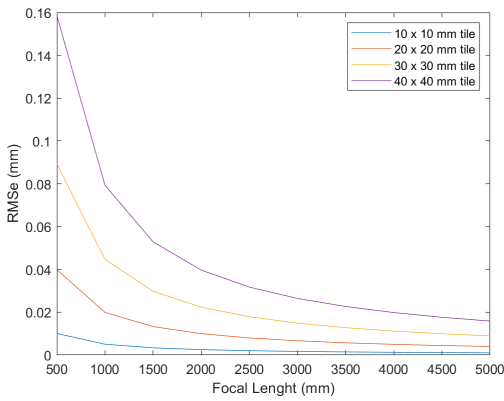


Figure 16. Minimum RMS error estimation of a flexure calculated by comparing a flat square tile of different sizes and different focal lengths (Right). The comparison is performed taking the RMS difference.

The dimensions of the spring that joins tiles together, which is function of tile size, along with the flexure thickness and material characteristics (i.e. yield strength and young modulus), will limit the allowable sag before any plastic deformation can be performed on the flexure. A finite element model was performed to study the stress on the flexure springs, caused by the deformation.

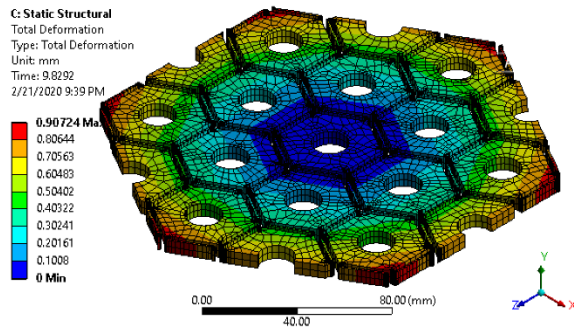


Figure 17. Finite Element Model performed in a section of stainless steel, 6 mm thick flexure showing the total deformation. The boundary condition was imposed with a zero displacement in the central hole, where displacements were imposed in selected edges accordingly to a parabola with focal length of 2.5 m. In the picture, showing a sag of 0.907 mm.

Future work will include an analytical model that allows for the characterization and prediction of the correct spring dimensions that will maximize the allowable sag without compromise to the integrity of the flexure. A prototype of a 1 x 1 m flexible mold is under development that includes a mechanism where the mold can be adjusted from the top surface (rather than the backing structure in the 50 cm mold) and including a spring mechanism to minimize variation caused by the swivels. More experiments are required to fully understand the characteristics of the flexure, with applications that include dynamic adjustment of the surface

to be used in secondary active optics for radio telescopes. Studies like fatigue and behavior under high temperatures are also required in future studies.

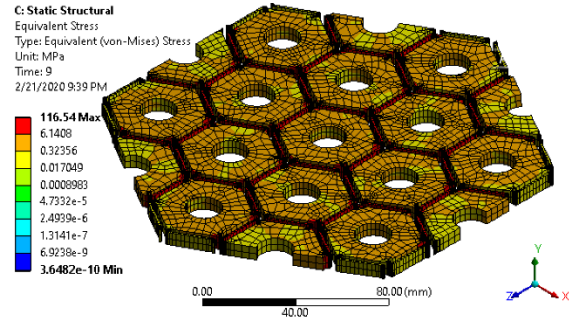


Figure 18. Finite Element Model showing the total equivalent stress with a 116 MPa maximum stress.

6. SURFACE METROLOGY

To verify that the desired shape is produced, a quick, robust, in-situ metrology method must be developed. The measurement method needs to have large dynamic range; being able to measure both concave and convex surfaces. For an acceptable characterization of the mirror panels for imaging applications, measurement RMS accuracy should ideally achieve $\sim\lambda/25$ for the shortest wavelength in use. For instance, ~ 1 mm wavelength radio telescope applications will require an RMS accuracy of $\sim 40 \mu\text{m}$.

Coherent light measurement methods like interferometry are ineffective for this task due to the diffuse surface roughness of the panels. Also, achieving null configuration for various panel shapes will be very challenging as they will require customized nulling optics or computer-generated holograms (CGHs).

We are considering two complimentary metrology systems as a primary and secondary metrology solution. Our team at the Wyant College of Optical Sciences has developed agile deflectometry metrology systems using He-Ne laser and thermal infrared (IR) radiation sources ($\sim 10 \mu\text{m}$ wavelength) that accurately measure glass and metal surfaces in the span of a few minutes. This technology was used during the grinding of the 4.2 m primary substrate for the Daniel K. Inouye Solar Telescope [17]. Dr. Kim's team further enhanced the IR deflectometry system and demonstrated a robust metrology solution for thermoformed aluminum panels (Figure 19) [18].

As a second approach, recent advancements in the calibration of fringe projection metrology (FPM) systems have brought measurement accuracy down from hundreds of microns [19] to tens of microns [20]. This makes FPM a perfect candidate for measuring large, diffuse, and varying aluminum panels at high speeds and high spatial resolutions. Only requiring a projector and a camera, this robust system can be implemented in nearly any environment.

FPM works on the principle of stereo vision (SV), which identifies the same point in space on two different detector arrays. With known properties of each camera (intrinsic parameters) and known properties of the camera positions relative to each other (extrinsic parameters), the 3D coordinates of each point seen in the overlapping fields of view of the cameras can be identified. However, SV suffers from noise in defining the same object between both camera sensors and therefore usually also requires fiducials to be placed to improve accuracy. FPM replaces a camera with a projector and leverages patterns to more accurately triangulate points and build high resolution 3D surface maps without the need for surface fiducials.

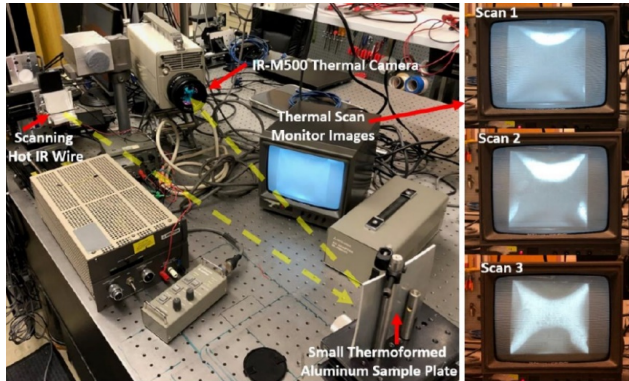


Fig. 19. IR deflectometry system measuring freeform sample panel. [18]

SUMMARY

A novel process to shape compound curve metallic sheets has been developed with potential applications in radio astronomy, architecture and aerospace industries. A short description of the current methods to manufacture radio telescope primary reflectors was presented, as well as an example of possible application in the radio telescope design. The electromagnetic thermoforming process is also described, with the principal equations that account for its modeling. The first experiment performed on a laboratory scale sample plate was also discussed. A parabolic shape with accuracy of 45 μm was produced in 1100 aluminum alloy from a 125 x 125 x 3 mm flat blank, finally two methodologies to perform the surface metrology were introduced: the IR deflectometry and the fringe projection metrology, which will be continue to be explored by the authors.

ACKNOWLEDGEMENTS

This material is based upon work supported by the National Science Foundation under Grant number 2009384. The authors thank Tech Launch Arizona for the financial support to perform this work with the Asset Development Grant. This research was made possible in part by the II-VI Foundation Block-Gift Program and the Technology Research Initiative Fund Optics/Imaging Program. Lastly to CONACYT - SENER fund "Fondo de Sustentabilidad energética", for its support.

DISCLOSURES

Authors Christian Davila-Peralta and Justin Hyatt have financial connections to Paramium Technologies LLC, a company that commercializes some of the technologies described in this paper.

REFERENCES

- [1] Valsecchi, G., Eder, J., Grisoni, G., Van Klooster, C., & Fanchi, L. (2003). High precision electroformed nickel panel technology for sub-millimeter radio telescope antennas. IEEE Antennas and Propagation Society International Symposium. Columbus: IEEE Xplore
- [2] Kildal, P.-S. (2013). Some reflector and feed antenna inventions that made a difference: Fundamentals and examples from radio telescopes, satellite communications and radio links. AFRICON 2013. Pointe-Aux-Piments: IEEE Xplore.
- [3] Cheng, J. (2009). Radio Telescope Design. In: The Principles of Astronomical Telescope Design. In Astrophysics and Space Science Library. New York, NY: Springer.
- [4] Baars, J. W., & Karcher, H. J. (2018). Radio Telescope Reflectors. Cham, Switzerland: Springer International Publishing AG.
- [5] Max Planck Institute for Radioastronomy. (2020, 02 05). Retrieved from Technical Data of the 100m-telescope: <https://www.mpifr-bonn.mpg.de/245888/specs>
- [6] Davila-Peralta, C., & Hyatt, J. (2019). USA Patent No. PCT/US19/57032
- [7] Liu, Y., Zhoujie, Z., Zijian, W., Bin, Z., Yilin, W., & Yishen, Z. (2018). Flow and friction behaviors of 6061 aluminum alloy at elevated temperatures and hot stamping of a B-pillar. The International Journal of Advances Manufacturing Technology, 4063-4083.
- [8] Favennec, Y., Labbe, V., & Bay, F. (2003). Induction heating processes optimization a general optimal control approach. Journal of computational physics 187, 68-94
- [9] Zinn, S., & Siematin, S. (1988). Elements of induction heating - Design, control and applications. ASM International.
- [10] Pysk, V., RIsch, D., Kinsey, B., Tekkaya, A., & Kleiner, M. (2011). Electromagnetic forming - A review. Journal of Materials Processing Technology 211, 787-829.
- [11] Buhler, H., & Bauer, D. (1968). A contribution to the deformation resistance of metallic materials during high-speed forming by means of magnetic fields. Bänder Bleche Rohre 9, 230 -234.

- [12] Xu, J., Su, J., Cui, J., Su, G., Liu, J., & Li, G. (2015). Thermal effects in magnetic pulse forming of magnesium alloy sheet. *Int J Adv Manuf Technol*, 755-770.
- [13] Mohan, S. S., Hershenson, M. d., Boyd, S. P., & Lee, T. H. (1999). Simple accurate expressions for planar spiral inductances. *IEEE Journal of Solid-State Circuits* 34, 1419 - 1424.
- [14] Nakagawa, Y., Mori, K.-i., Yashima, S., & Kaido, T. (2018). Springback behaviour and quenchability in hot stamping of thick sheets. 17th International Conference on Metal Forming (pp. 1071-1078). Toyonashi: Procedia Manufacturing.
- [15] Angel, R. P., & Stalcup, T. E. (2017). USA Patent No. US 2017 / 0369355 A1.
- [16] Davila-Peralta, C. & Hyatt, J. J., (2019). PCT/US19/57032.
- [17] Kim, D. W., Su, P., Oh, C. J., & Burge, J. H. (2015, August). Extremely large freeform optics manufacturing and testing. In *Conference on Lasers and Electro-Optics/Pacific Rim* (p. 26F1_1). Optical Society of America.
- [18] Kim, Dae Wook; Smith, Greg; Dubin, Matt; Lowman, Andrew; Oh, Chang-Jin; Quach, Henry; Kang, Hyuk Mo; Yoo, Hyemin; Trumper, Isaac; Graves, Logan; Aftab, Maham; Davila, Christian; Hyatt, Justin; Choi, Heejoo, "Advances in reconfigurable optical design, metrology, characterization, and data analysis," *J. Phys. Photonics* (IOP) (2020). (In press)
- [19] Zhang, Song, and Peisen S. Huang. "Novel method for structured light system calibration." *Optical Engineering* 45.8 (2006): 083601.
- [20] Vargas, Raúl, et al. "Hybrid calibration procedure for fringe projection profilometry based on stereo vision and polynomial fitting." *Applied Optics* 59.13 (2020): D163-D169.

BIOGRAPHY



Christian Davila-Peralta received a B.S. in Engineering from ITESM in 2009, a Masters on Systems and Industrial Engineering from the University of Sonora in 2013, and a Masters of Science in the University of Arizona in 2018. He has been with the Steward Observatory for 5 years, while studying his PhD in Mechanical Engineering at the Mechanical and Aerospace Engineering Department.



Justin Hyatt is a researcher in the University of Arizona's Steward Observatory. His research includes radio astronomy instrumentation, satellite communication, and fabrication and metrology of freeform metallic reflectors. He received his PhD in Optical Sciences and a double bachelors degree in Mechanical Engineering and English.



Joel Berkson received a B.S in Optical Sciences and Engineering in 2019 and is currently in his 2nd year pursuing a PhD in Optical Sciences at the James C. Wyant College of Optical Sciences. His research interests are optical metrology, optical system design, and analysis.



Zack Hatfield received a B.S in Optical Sciences and Engineering in 2020 and is currently in his final year pursuing a MS in Optical Sciences at the James C. Wyant College of Optical Sciences. His research interests include astronomical instrumentation, optical system design, and optical testing/metrology.



Alex St. Peter is an undergraduate research assistant at the University of Arizona pursuing a B.S in Optical Sciences and Engineering. His research interests include optical system design and analysis, surface finishing, and computer aided design.



Bailey S. Allen is an undergraduate research assistant at the University of Arizona pursuing a B.A in English and pre-requisites for her Doctorate in Audiology. Her research interests include induction for use in the thermoforming process, as well as technical writing and analysis.



Wyatt Ellis is an undergraduate research assistant at the University of Arizona. He is currently pursuing a B.S. in Physics and a B.S. in Aerospace Engineering. His research interests include space systems, astronomical instrumentation, and materials science.



Naomi Nguyen is an undergraduate research assistant at the University of Arizona pursuing a B.S in Mathematics and a B.S in Computer Science. Her research interests include mathematical modeling, data analysis, and computer programming.



Emily Rodriguez is an undergraduate research student at the University of Arizona. She is currently pursuing a B.S in Optical Sciences and Engineering. Her research interests include optical metrology and computer programming.



Dae Wook Kim is an assistant professor of optical sciences and astronomy at the University of Arizona. His research area covers precision optical engineering, including interferometry and deflectometry. He is the chair of the Optical Manufacturing and Testing (SPIE) and Optical Fabrication and Testing (OSA) conferences. He is a senior member of OSA and SPIE and has served as an associate editor for the OSA Optics Express journal.